RSC Advances

PAPER

View Article Online
View Journal | View Issue

Cite this: *RSC Adv.*, 2017, **7**, 37568

Facile synthesis of Au@Ag–hemin decorated reduced graphene oxide sheets: a novel peroxidase mimetic for ultrasensitive colorimetric detection of hydrogen peroxide and glucose†

Sanjay Kumar,[a] Pulak Bhushan[a] and Shantanu Bhattacharya*[ab]

Herein we report the facile synthesis of a quaternary nanocomposite material (hemin–silver coated gold–graphene oxide) and evaluate its efficacy as a novel peroxidase mimetic. A strong synergistic coupling between the various components involved results in an excellent catalytic performance of this nanocomposite. A comparison of the different morphologies of the silver coated gold particles strongly indicates a greater sensitivity of the nanostar morphology over the nanoparticle morphology owing to its high surface-to-volume ratio. Furthermore, the immobilization of hemin and silver coated gold nanostars on a graphene oxide sheet framework imposes a nanoscale confinement, effectively augmenting the overall catalytic performance of the composite. The nanocomposite followed typical Michaelis–Menten theory and electrochemical analysis suggested facilitation of accelerated electron transfer between TMB and H_2O_2. A K_M value of 2.75 mM^{-1} suggested a high affinity of the nanocomposite towards TMB. Furthermore, a 2.8 times increase in the maximum reaction rate compared to HRP established the high catalytic activity of the nanocomposite. The nanocomposite demonstrates a nanomolar range sensitivity towards hydrogen peroxide and glucose (limit of detection = 1.26 nM and 425 nM). The nanocomposites have also been employed to develop a paper-based point-of-care diagnostic device. The device has been utilized for detection of glucose in human blood serum samples with satisfactory results.

Received 22nd June 2017
Accepted 25th July 2017

DOI: 10.1039/c7ra06973a

rsc.li/rsc-advances

Introduction

Enzymes are biological catalysts serving a wide variety of disciplines in the paper, chemical and food processing industries, biochemical and medical fields, *etc.* Natural enzymes are extensively used as catalysts owing to their high catalytic efficiency and substrate specificity. However, their extreme susceptibility to denaturation in stringent conditions restricts their practical applications. Moreover, their complicated and expensive synthesis and storage has led to immense interest in discovering artificial enzyme mimetics.[1] Hemin,[2–4] cyclodextrin,[5] porphyrin,[6] graphene oxide,[7,8] metal nanoparticles,[9–11] *etc.*, have attracted immense attention for the development of enzyme mimetics. Hemin, a natural metalloporphyrin and the active center of heme proteins, which include cytochromes, peroxidases, myoglobins and hemoglobins, exhibits a peroxidase-like activity.[3,12] Nevertheless, it suffers from poor catalytic activity due to oxidative self-degradation, molecular aggregation to yield inactive dimers and low solubility in aqueous buffers.[13] Immobilization of hemin on high surface area materials has led to improved efficiency by the virtue of effective site isolation.[14]

Metal nanoparticles like gold, silver, *etc.* also possess unique catalytic activity accounted to their large surface area and other quantum effects. The intricate interplay between their surface structures, morphology and optical properties befit them for their deployment as chemical and biological sensors. These nanoparticles exhibit local surface plasmon resonance effect (LSPR), in which localized electromagnetic field peaks on a metallic surface on excitation by an incident light of specific wavelength. This effect is extremely sensitive to the morphology of the nanoparticles, their aggregation behavior and their engulfing surrounding media.[15,16] Benefitting from these advantages, a variety of metal nanoparticles and their hybrids have been recently found to show excellent peroxidase-like activity, for example, AuNPs,[17,18] AgNPs,[19] Au@Ag core–shell NPs,[20] chitosan-stabilized AgNPs,[9] DNA–Ag/Pt nanoclusters,[21] *etc.* Furthermore, an investigation into the nanoparticle morphology reported that nanoparticles with an overall lower symmetry possess a very high field enhancement factor.[22] Recent technological advancements in the synthesis of

[a]*Microsystems Fabrication Laboratory, Department of Mechanical Engineering, Indian Institute of Technology Kanpur, India. E-mail: bhattacs@iitk.ac.in*

[b]*Design Programme, Indian Institute of Technology Kanpur, India*

† Electronic supplementary information (ESI) available. See DOI: 10.1039/c7ra06973a

nanoparticles have enabled the fabrication of anisotropic nanoparticles such as nanorods, nanotubes, nanoshells and nanostars. Among these, nanostars have received considerable attention owing to their distinguished characteristics such as wide range of tunable LSPR, excellent surface-enhanced Raman scattering (SERS) performance, superior optical detectability, multipeak scattering and high surface-to-volume ratio.[23,24] Gold nanoparticles (AuNPs) have played a critical role in this domain owing to their excellent optical properties, biocompatibility and facile synthesis. In the past few decades, several efforts have been made to augment the catalytic activity and stability of AuNPs. An interesting approach has been coating of the gold nanoparticles with silver. The intrinsic properties of silver nanoparticles like higher extinction coefficient, higher scattering to extinction ratio and sharp extinction bands, result in the bimetallic nanoparticles having a broader plasmon resonance band than that of individual nanoparticles.[25,26] Silver nanoparticles have been known to be effective scavengers of H_2O_2. However, their optical properties are rarely utilized albeit their high catalytic activity, owing to their self-coalescing property. Hence, a nanocomposite of Au@Ag can result in both superior catalytic activity and unique optical properties.

Recently, graphene oxide has also been reported to possess intrinsic peroxidase-like catalytic activity.[7] On account of its high surface area and rapid electron transfer capability, it has been widely used as an anchoring substrate for various nanomaterials like gold/silver nanoparticles, hemin, iron oxide, *etc.* to enhance their catalytic efficiency.[27,28] However, exploration of superior enzyme mimetics with higher stability and sensitivity is vital for the advancement of the biomimetic field. In addition, colorimetric detection techniques based on such artificial enzyme mimetics could facilitate a substantial improvement in the detection limits. Such techniques can allow for rapid, robust and inexpensive detection of various biomarkers obviating the need for laboratory sample evaluation.

Herein, we have reported synthesis of a simple quaternary nanocomposite of gold, silver, hemin and graphene oxide (Au@Ag–H–rGO). The nanocomposite is an ensemble of graphene oxide serving as a matrix for anchoring hemin and silver coated gold nanoparticles/nanostars. A surface coating of silver helped enhance the stability of gold nanoparticles and may have changed its surface properties leading to a higher catalytic activity. Further, a synergistic interaction between the Au@Ag nanocomposites and hemin with graphene oxide led to a highly stable catalytic nanozyme. Interestingly, an investigation on the shape-dependent sensitivity of gold revealed that, the star-shaped morphology exhibit superior performance and stability over the spherical-shaped morphology. The synthesized nanocomposites are found to efficiently oxidize the peroxidase substrate TMB in the presence of H_2O_2, exhibiting an overall excellent catalytic activity. The exploitation of the nanostar morphology amalgamated with the embedment over GO sheet led to the development of a highly sensitive and selective colorimetric sensor for H_2O_2. It is known that H_2O_2 is produced by many oxidative enzymes (*e.g.* glucose, cholesterol, uric acid) when reacted with suitable substrates. The quantification of these enzymes depends on the amount of H_2O_2 produced in the reaction, necessitating its detection in trace amounts. Among these oxidative enzymes, glucose is a crucial biomarker for diagnosis of diseases like diabetes,[29] cancer,[30] *etc.* Hence, the H_2O_2 detection mechanism was further employed for the determination of glucose in human serum samples. The system showed high selectivity and sensitivity along with good reproducibility towards glucose, showing great potential for clinical diagnosis for future use. Exploiting this detection mechanism, a paper-based sensing platform was implemented for rapid and visual on-site monitoring of glucose in human serum samples.

Experimental section

Materials and reagents

Graphite flakes (acid treated, ≥99%), sodium chloride (NaCl), sulphuric acid (H_2SO_4, ≥98%), potassium permanganate ($KMnO_4$, ≥99%), hydrogen peroxide (30 wt% in H_2O), glucose oxidase (GOx), D-glucose, hydrochloric acid (35%), acetic acid, sodium acetate trihydrate ($CH_3COONa \cdot 3H_2O$, ≥99%), ammonia solution, tri-sodium citrate dihydrate ($C_6H_5Na_3O_7 \cdot 2H_2O$, ≥99%), sodium borohydride ($NaBH_4$, ≥98%), silver nitrate ($AgNO_3$, ≥99%), hemin, cetyltrimethyl ammonium bromide (CTAB, ≥98%) and Whatman qualitative filter paper grade 1 were purchased from Sigma Aldrich, India. Gold(III) chloride trihydrate ($HAuCl_4 \cdot 3H_2O$, ≥99.9%), L-ascorbic acid (≥99%) and 3,5,3′,5′-tetramethylbenzidine (TMB) were obtained from Loba Chemie Pvt. Ltd., India. All chemicals and reagents used were of analytical grade. All aqueous solutions were prepared in high performance liquid chromatography (HPLC) water. Human blood serum samples were obtained from IIT Kanpur, India, and all analyses were performed at the Microsystems Fabrication Laboratory. All experiments were performed in compliance with the relevant laws and national guidelines (Ethical Guidelines for Biomedical Research on Human Participants, provided by Indian Council of Medical Research), and the ethical clearance for the same was provided by the GSVM Medical College, Kanpur. All the experiments with the samples were performed with informed consent obtained from the persons who provided the samples.

Synthesis of AuNP@Ag–hemin–rGO and AuNS@Ag–hemin–rGO nanocomposites

Synthesis of hemin–rGO. Graphene oxide was synthesized using the modified Hummer's method.[31] H–rGO was prepared by following standard procedure.[32] Briefly, 10 mg of GO was mixed with 20 mL of HPLC water in a flask and ultrasonicated for 30 min at room temperature. Next, 20 mL of hemin aqueous solution (0.5 mg mL^{-1}) was added, followed by an addition of 200 μL of ammonia solution. Then, 30 μL hydrazine hydrate was added dropwise to the above solution. The resulting solution was vigorously stirred for 10 min and then refluxed at 60 °C for 4 h. Further, the solution was filtered and washed through repeated centrifugation with HPLC water. The final solution was stored at 4 °C until use.

Synthesis of gold nanostar/nanoparticle (AuNS/AuNP). AuNSs were prepared using a seed mediated growth approach according to a previously reported procedure.[24] In brief, to produce 12 nm gold seed solution, 100 mL of 1 mM $HAuCl_4$ aqueous solution was boiled under vigorous stirring, and then 15 mL of 1% tri-sodium citrate dihydrate aqueous solution was added. The resultant solution was kept boiling and stirring for an additional 15 min and was then cooled to room temperature in an ice bath. After filtration through a nitrocellulose membrane (pore size, 0.22 μm), the solution was stored at 4 °C. Gold nanostars were prepared by consecutive additions of 10 mL $HAuCl_4$ (0.5 mM), 10 μL 1 N HCl, 50 μL ascorbic acid (0.1 M) and 100 μL $AgNO_3$ (1 mM). 100 μL of the gold seed solution was added while continuously stirring the above solution. The solution was further stirred for 15 minutes followed by an addition of a 100 μL, of 0.1 M CTAB solution and additional stirring was carried out for 5 min. The resulting solution was then centrifuged at 5000 rpm for 30 min at 4 °C and the supernatant was discarded. The as-prepared AuNSs were re-dispersed in 10 mL of CTAB solution (1 mM) for further use. Gold nanoparticles (AuNPs) of size 30 nm were synthesized using the kinetically controlled seeded growth strategy.[33]

Synthesis of silver coated gold nanostar/nanoparticle (AuNS@Ag/AuNP@Ag). Three different kinds of AuNS@Ag nanocomposites were prepared by adding 0.1 M of $AgNO_3$ in different volumes (5, 10, and 15 μL) to a 1 mL AuNS solution. The samples were denoted as AuNS@Ag-5, AuNS@Ag-10 and AuNS@Ag-15. $AgNO_3$ was reduced through an addition of an equivalent volume of ascorbic acid (0.1 M) and 2 μL of NH_4OH. The color of the solution was found to darken out within the first 5 minutes of the mixing. The stabilization of the dark color in this case turn out to be an indicator for the successful completion of the reaction. The preparation of AuNP@Ag nanocomposites was similar to AuNS@Ag, with an exception of AuNP solution added in place of AuNS solution. AuNP@Ag nanocomposites were prepared only with 5 μL $AgNO_3$, and depicted as AuNP@Ag-5.

Synthesis of AuNP@Ag–hemin–rGO/AuNS@Ag–hemin–rGO. The wet-chemical method was utilized for the synthesis of final AuNP@Ag–H–rGO/AuNS@Ag–H–rGO nanocomposites. In the process, an equal amount of AuNP@Ag/AuNS@Ag nanocomposite and H–rGO was mixed and diluted with 10 mL of HPLC water. The mixture was ultrasonicated for 12 h. The prepared solution was filtered and washed through repeated centrifugation using HPLC water and vacuum dried to obtain the final AuNP@Ag–H–rGO/AuNS@Ag–H–rGO nanocomposites (Scheme 1).

Characterization

UV-visible spectra (UV-vis) were measured using an Evolution 300 spectrophotometer (Thermo Scientific). High resolution TEM (HR-TEM) and scanning-transmission-electron microscopy (STEM) images were recorded using a FEI Titan G2 60-300 TEM operated at 300 kV. The X-ray diffractometry (XRD) was performed on a Bruker D8 Advance X-ray diffractometer with Cu Kα ($k = 0.154$ nm) radiation (Bruker AXS, Germany). The Raman spectra were recorded on a confocal Raman microscope with 10× objective using an excitation laser light of wavelength 532 nm. Energy dispersive X-ray spectroscopy (EDS) (Oxford instruments) in conjunction with Sigma Field Emission Scanning Electron Microscope (CARL ZEISS) was used for chemical microanalysis of nanocomposites. Dynamic light scattering (DLS) and zeta potential measurements were carried out on a Beckman Coulter Delsa Nano C. Thermogravimetric analysis (TGA) profiles were obtained between 20 °C and 650 °C in O_2 using a Simultaneous Thermal Analyzer (STA) 8000 (Perkin Elmer Ltd.) instrument. The cyclic voltammetry measurements were carried out by BASi Epsilon Eclipse™. The pH values of the buffer solutions were recorded using a Labman benchtop pH

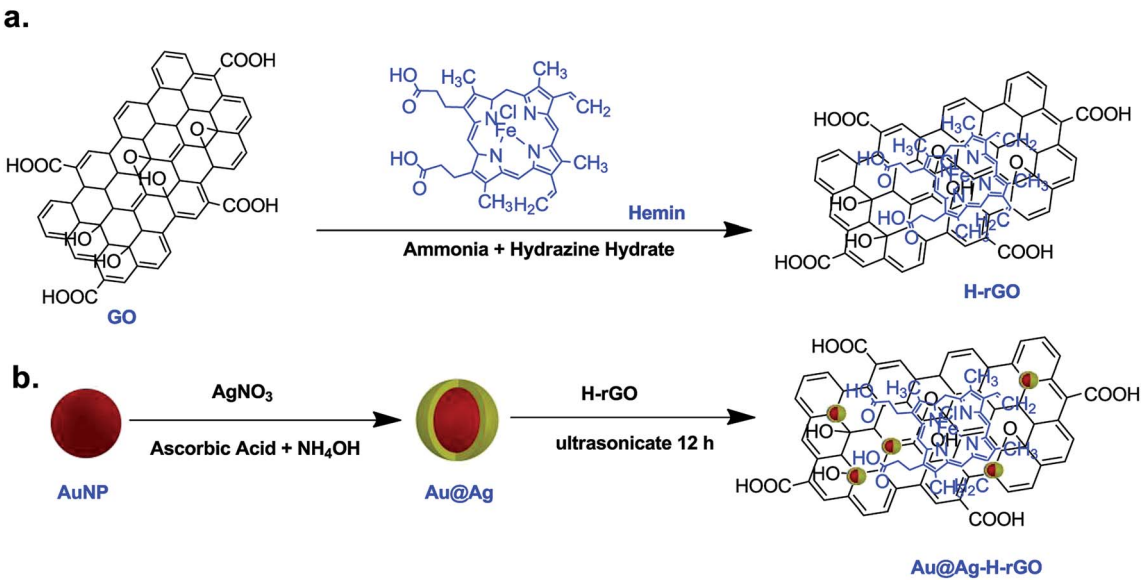

Scheme 1 Schematic representation of the synthesis of H–rGO and AuNP@Ag–H–rGO.

meter. Particle sizes were measured by image analysis of the TEM images using ImageJ software. Photographs of the samples in cuvettes and on paper were taken using a Nikon D3200 digital camera.

Catalytic activity and kinetic state assays of AuNP/AuNS@Ag–H–rGO

In order to study the catalytic activity of the synthesized nanocomposites, 500 μL of 600 μM TMB and 500 μL of AuNP/AuNS@Ag–H–rGO (0.5 μg mL^{-1}) solution was mixed in 0.02 M sodium acetate–acetic acid buffer (pH = 4.1) and vortexed for 10 min. Next, 1 mL of H_2O_2 solution (0.5 mM) was added to above solution. To analyze the steady state kinetics of the reaction, 500 μL of AuNP/AuNS@Ag–H–rGO (0.5 μg mL^{-1}) mixed with 500 μL TMB or H_2O_2 (60 μM) as substrate was used. The solution was diluted in sodium acetate–acetic acid buffer (0.02 M). The spectral measurements were recorded at 652 nm using which the maximal reaction rate and the Michaelis–Menten constant were calculated.

Colorimetric detection of H_2O_2 and glucose

For H_2O_2 measurements, 500 μL TMB (60 μM) and 500 μL of AuNP/AuNS@Ag–H–rGO (0.5 μg mL^{-1}) solution was mixed in 0.02 M sodium acetate–acetic acid buffer (pH = 4.1) and vortexed for 10 min. 1 mL of H_2O_2 of varying concentrations (10, 15, 20, 25, 35, 50, 75 and 100 nM) was added to the above solution, after which the spectral measurements were carried out. For glucose detection, the colorimetric detection mechanism of H_2O_2 was utilized based on the catalytic oxidization of glucose by GOx (glucose + O_2 + GOx → gluconic acid + H_2O_2). In a typical experiment, a mixture of 50 μL of the as-synthesized AuNS@Ag–H–rGO nanocomposites (0.5 μg mL^{-1}) and 20 μL of TMB (1 mM in methanol) was added to 3 mL of 0.02 M sodium acetate–acetic acid buffer (pH = 4.1) solution. Then, 15 μL of GOx aqueous solution (1 mg mL^{-1}) and 150 μL of glucose with various concentrations (2, 3, 5, 10 and 15 μM) in sodium phosphate buffer (0.1 mM, pH = 7) were mixed to the above solution.

Electrochemical study of AuNP/NS@Ag–H–rGO

For conducting the electrochemical measurements, the glassy carbon electrodes (GCEs) were polished subsequently with 0.3 and 0.05 μm alumina slurry, rinsed with HPLC water, washed successively with ethanol and HPLC water in an ultrasonic bath and dried in air. Then, the AuNP/AuNS@Ag–H–rGO modified GCEs were prepared by dropping 10 μL of AuNP/AuNS@Ag–H–rGO (3 μg mL^{-1}) solution on the surface of the GCE, and air dried overnight.

Preparation of human blood serum samples

To demonstrate the practical feasibility of the proposed detection assay, three human blood samples were collected and analyzed. All samples were centrifuged at 2000 rpm for 10 min to extract the serum. The supernatant was then diluted 20 times using sodium phosphate buffer (0.1 mM, pH = 7). Further, the samples were spiked with known concentrations of glucose to establish the selectivity of the assay.

Results and discussion

Characterization of the AuNP/AuNS@Ag–hemin–rGO

To monitor the successful synthesis of the nanocomposites, UV-visible spectroscopy (UV-vis) was utilized at every step. The spectrum of Au seeds showed an absorption maximum at 517 nm, confirming the synthesis of 12 nm sized particles (Fig. S1†). The absorption spectra of rGO, hemin and H–rGO are shown in Fig. S2a.† An aqueous dispersion of rGO exhibits a strong peak at 272 nm. In case of pure hemin the strong peak at 385 nm can be ascribed to the Soret band and a broad weak peak around 600 nm assigned to the Q-bands. Further, a red shift of the Soret band from 385 nm to 395 nm is observed in the H–rGO spectrum, which may be attributed to the ring π–π* transitions of the Soret band. This may be inferred as an interaction between the porphyrin moiety and the rGO sheet.[34] Fig. S2b† illustrates the UV-vis spectra of AuNPs and AuNSs coated with varying amounts of silver, along with TEM images of a few representative samples. Initially, AuNPs and AuNSs showed respective strong peaks at 527 nm and 582 nm. But, with the increasing amount of coated silver, a progressive blue-shift in the surface plasmon wavelength has been observed. For example, the peak at 582 nm corresponding to AuNSs has been blue shifted to 437 nm on addition of 5 mL of silver nitrate. It has been observed from the TEM images that the silver first grows over the core region of the AuNS core and then over its branches. It has been seen that using a lower amount of Ag leads to the synthesis of AuNS structure with exposed branches. Hence, all the subsequent experiments and characterization were performed using AuNP@Ag-5–H–rGO and AuNS@Ag-5–H–rGO. The UV-vis spectra of AuNP@Ag–H–rGO and AuNS@Ag–H–rGO are presented in Fig. 1. The spectra showing prominent peaks of 270 and 385 nm confirms to the presence of rGO and

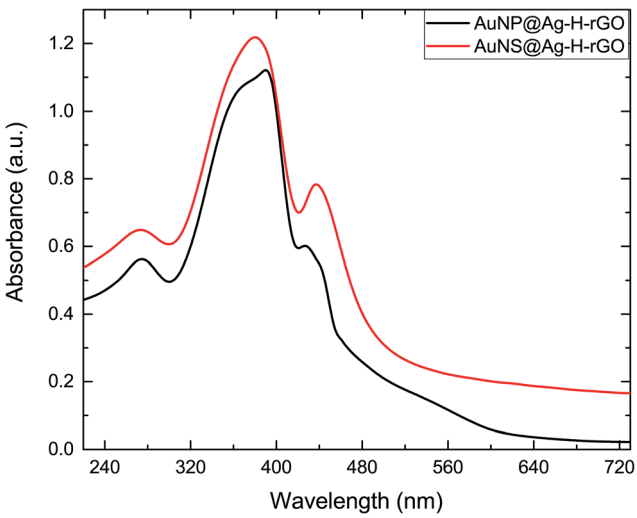

Fig. 1 UV-vis absorption spectra of the as-synthesized nanocomposites.

hemin in the structures. In addition, the peaks at 428 and 437 nm correspond to AuNP@Ag and AuNS@Ag respectively. Fig. S3a and b† show the folded morphology of the single-layered rGO sheet and the successful adsorption of hemin over its surface respectively. The crystalline nature of rGO is represented by the SAED patterns shown as insets. Fig. S3c and d† illustrate the TEM images of as-synthesized AuNPs and AuNSs. The images revealed an average size of the AuNPs to be 30 nm and the AuNS core has been measured to be 20 nm with an average branch length of 15 nm. Fig. S4a and b† reveal the STEM images of AuNS@Ag and AuNS@Ag–H–rGO and the presence of the constituent elements have been further confirmed by elemental mapping using EDS technique. The TEM images of AuNP@Ag show an average size distribution of 50 nm of the synthesized gold nanoparticles. The silver coating over the gold nanoparticles can be clearly seen in the image inset (Fig. 2a). Fig. 2b shows the TEM image of silver coated gold nanostars. The crystallinity of the particles was established by the well-defined diffraction patterns (inset). Fig. 2c and d illustrate the morphology of the as-synthesized nanocomposites by TEM where, AuNP@Ag/AuNS@Ag and hemin can be seen localized and well dispersed over the rGO sheets. The acquired SAED patterns of the same confirm the crystalline structure of the nanocomposites (insets). H–rGO and AuNS@Ag–H–rGO nanocomposites have been further identified using X-ray diffraction (XRD) patterns as shown in Fig. 3a. The characteristic peaks corresponding to (002) at angle 22.82° confirms the existence of hexagonal structure of rGO. Further, five diffraction peaks (111), (200), (220), (311) and (222) confirms face centered cubic structure of Au and Ag (PDF 00-004-0783, PDF 00-004-0784). The diffraction peaks of gold and silver show high overlap with each other mostly owing to their similar lattice constants (Au = 0.4080 nm and Ag = 0.4086 nm).[35] Shown in Fig. 3b is the Raman spectra of AuNP@Ag–H–rGO and AuNS@Ag–H–rGO nanocomposites. In its non-aggregated state, the AuNS@Ag–H–rGO shows approximately 2.5 ± 0.2 times higher signal intensity compared to AuNP@Ag–H–rGO. A major signal enhancement has been observed along with a blue-shift in the Raman band at five peaks corresponding to 299, 481, 712, 1309, 2436 cm^{-1} implying a synergistic interaction between H–rGO and AuNS@Ag. Energy dispersive X-ray spectroscopy (EDS) was utilized to analyze the elemental distribution of the as-synthesized nanocomposite (Fig. S5†). The peaks of Au, Ag, Cl and Fe suggested successful loading of hemin and AuNS@Ag on the rGO sheets. A strong negative charge of 24 mV and 57 mV revealed by zeta potential analysis indicated the high colloidal stability of AuNP@Ag–H–rGO and AuNS@Ag–H–rGO as a result of the acting intermolecular repulsion forces (Fig. S6†). The loading content of hemin, AuNP@Ag and AuNS@Ag calculated using thermal gravimetric analysis (TGA), was found to be about 10 wt%, 29 wt% and 30 wt% respectively (Fig. S7†).

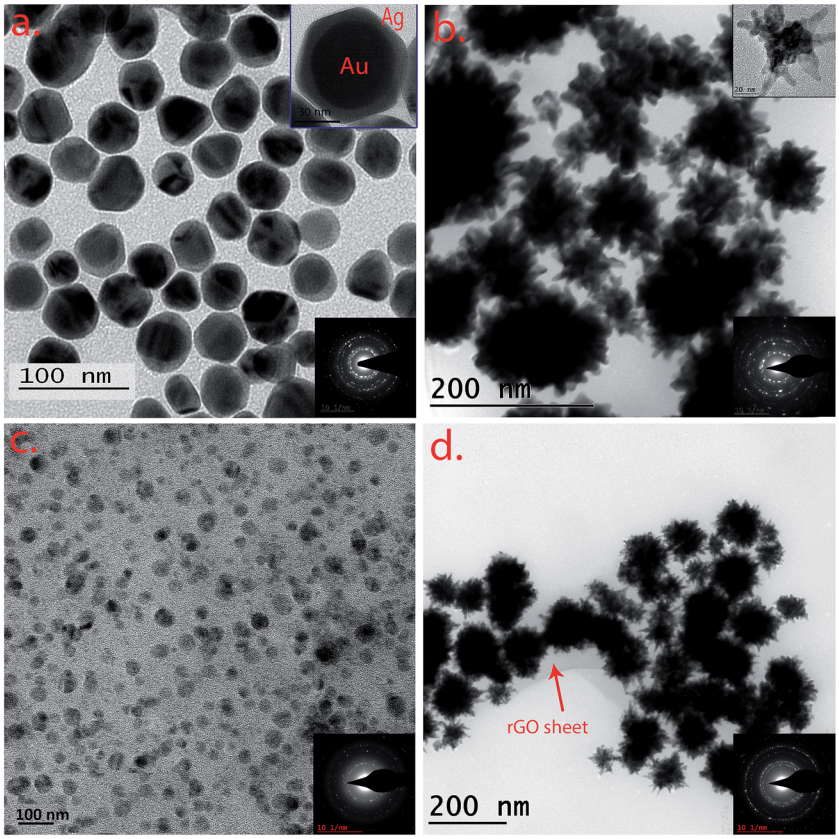

Fig. 2 TEM images of (a) AuNP@Ag, (b) AuNS@Ag, (c) AuNP@Ag–H–rGO and (d) AuNS@Ag–H–rGO nanocomposites. Lower insets are respective SAED patterns and the upper insets are the respective TEM images at higher magnification.

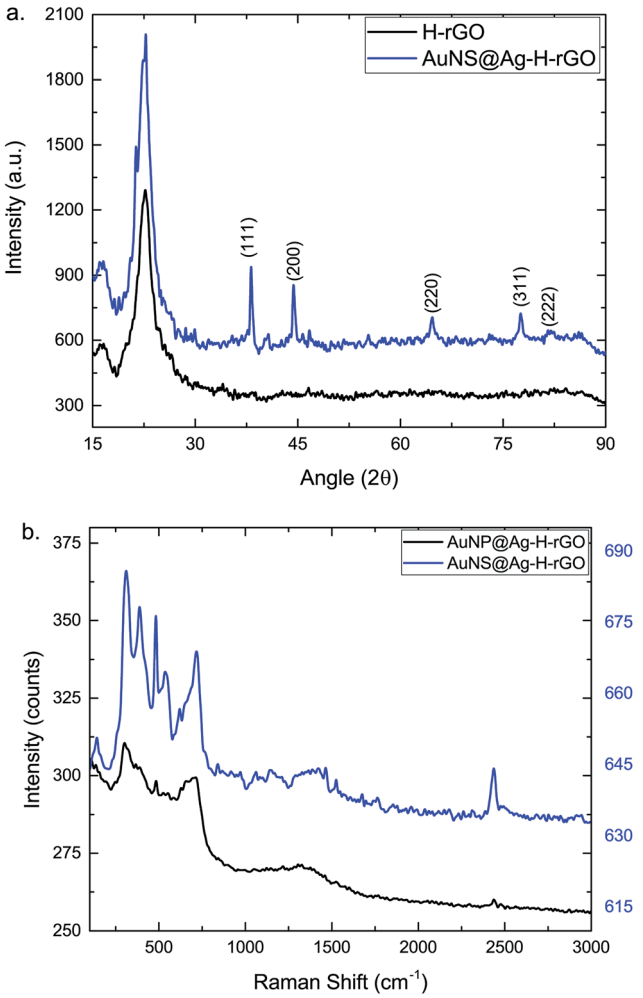

Fig. 3 Structural characterization of the as-synthesized nanocomposites (a) XRD and (b) Raman.

Catalytic activity of AuNP/AuNS@Ag–H–rGO

To evaluate the peroxidase-like activity of the as-prepared AuNP/AuNS@Ag–H–rGO nanocomposites, the catalysis of peroxidase substrate TMB in presence of H_2O_2 was tested and monitored by UV-vis spectroscopy (Fig. S8†). The catalytic properties of 10 wt% hemin in H–rGO, 29 wt% AuNP@Ag, 30 wt% AuNS@Ag and the final nanocomposites AuNP/AuNS@Ag–H–rGO were investigated. An addition of H_2O_2 to a solution mixture of TMB and AuNP/AuNS@Ag–H–rGO resulted in an overall blue coloration of the solution. In the absence of the synthesized nanocomposites, the absorbance was quite low and an SPR effect was observed at 652 nm, corresponding to oxidized TMB.[36] On addition of H–rGO, an increase in the absorbance was observed, similar to when AuNP/AuNS@Ag was added. Since the loading of AuNP@Ag and AuNS@Ag was similar, it can be safely inferred from the graph that the nanostar morphology led to a higher catalytic activity than that of spherical morphology. Addition of AuNP@Ag–H–rGO showed a stronger catalytic activity, whilst, in the presence of the AuNS@Ag–H–rGO, the absorbance value was increased ten times. This confirmed a synergistic interaction between H–rGO and AuNS@Ag leading to a dramatic stimulation in the catalytic activity of the nanocomposites.

The intrinsic peroxidase-like activity of AuNP/AuNS@Ag–H–rGO nanocomposites was further optimized by analyzing the effect of physical reaction conditions like pH, temperature and concentration of H_2O_2 on their catalytic efficiency (Fig. S9a–c†). The optimum values for pH, temperature and H_2O_2 concentration obtained were 4.1, 37 °C and 150 μM corresponding to which the maximum catalytic efficiency would be demonstrated. Thus, subsequent experiments were performed under these optimized set of conditions. Next, to investigate the catalytic activity of the as-synthesized nanocomposites, the steady state kinetics of the reaction was analyzed. Fig. 4a, b, S10a and b† show the time-dependent absorbance changes of the reaction solution at 652 nm with H_2O_2 and TMB as the substrates for AuNS@Ag–H–rGO and AuNP@Ag–H–rGO respectively. The typical Michaelis–Menten curves were obtained by evaluating the slopes (Fig. 4c, d, S10c and d†). Based on the calculated reaction rates, linear double reciprocal plots (Lineweaver–Burk plot) were acquired as shown in Fig. 4e, f, S10e and f.† These were used to find out the Michaelis–Menten constant (K_M) and maximum reaction rate (V_{max}). The slopes of all lines were parallel, indicating a characteristic ping-pong mechanism, as observed for native peroxidase (HRP).[37] This indicates that the nanocomposites first bind and react with the first substrate, yielding the first product and then react with the second substrate.

As is evident from Table 1, the apparent K_M values of 0.048 (TMB) and 2.75 (H_2O_2) for AuNS@Ag–H–rGO indicated its higher affinity to the substrates compared to AuNP@Ag–H–rGO which has K_M values of 0.062 (TMB) and 2.82 (H_2O_2). This infers that both the nanocomposites exhibit higher affinity to TMB compared to H_2O_2. Also, the higher affinity of AuNS@Ag–H–rGO can be attributed to the surface morphology of the AuNS@Ag providing a higher surface-to-volume ratio as compared to AuNP@Ag. Further, the rGO sheet acts as a supporting matrix for hemin and AuNS@Ag inhibiting their self-aggregation. Moreover, it confines them in a region which is of nanometric dimensions allowing for the efficient adsorption of the substrates and also improving the catalytic efficiency. The V_{max} of the synthesized nanocomposites showed a 2.8 and 2.1 times increase compared to HRP with TMB as the substrate. As a result of the superior performance of AuNS@Ag–H–rGO, the morphology of AuNS@Ag was further optimized and catalytic performance was evaluated for each of the morphologies. The amount of silver coating on the AuNSs was varied to achieve maximum sensitivity. Fig. S9d† corroborated that AuNS@Ag with an amount of 5 μL of Ag (*i.e.* AuNS@Ag-5), showed highest catalytic activity. This could be attributed to the fact that with Ag growing mainly on the core, the branches of the Au nanostar remain accessible, hence providing a higher surface-to-volume ratio for bioconjugation of TMB.

Henceforth, a colorimetric method was developed benefitting from the excellent catalytic activity of the synthesized nanocomposites. The response curves for a mixture of nanocomposites and TMB with varying concentrations of H_2O_2 were obtained (Fig. 5a and c). It was discerned that an increase in the H_2O_2 concentration led to an overall increase in the absorbance. Fig. 5b and d present the linear calibration plot for the varying

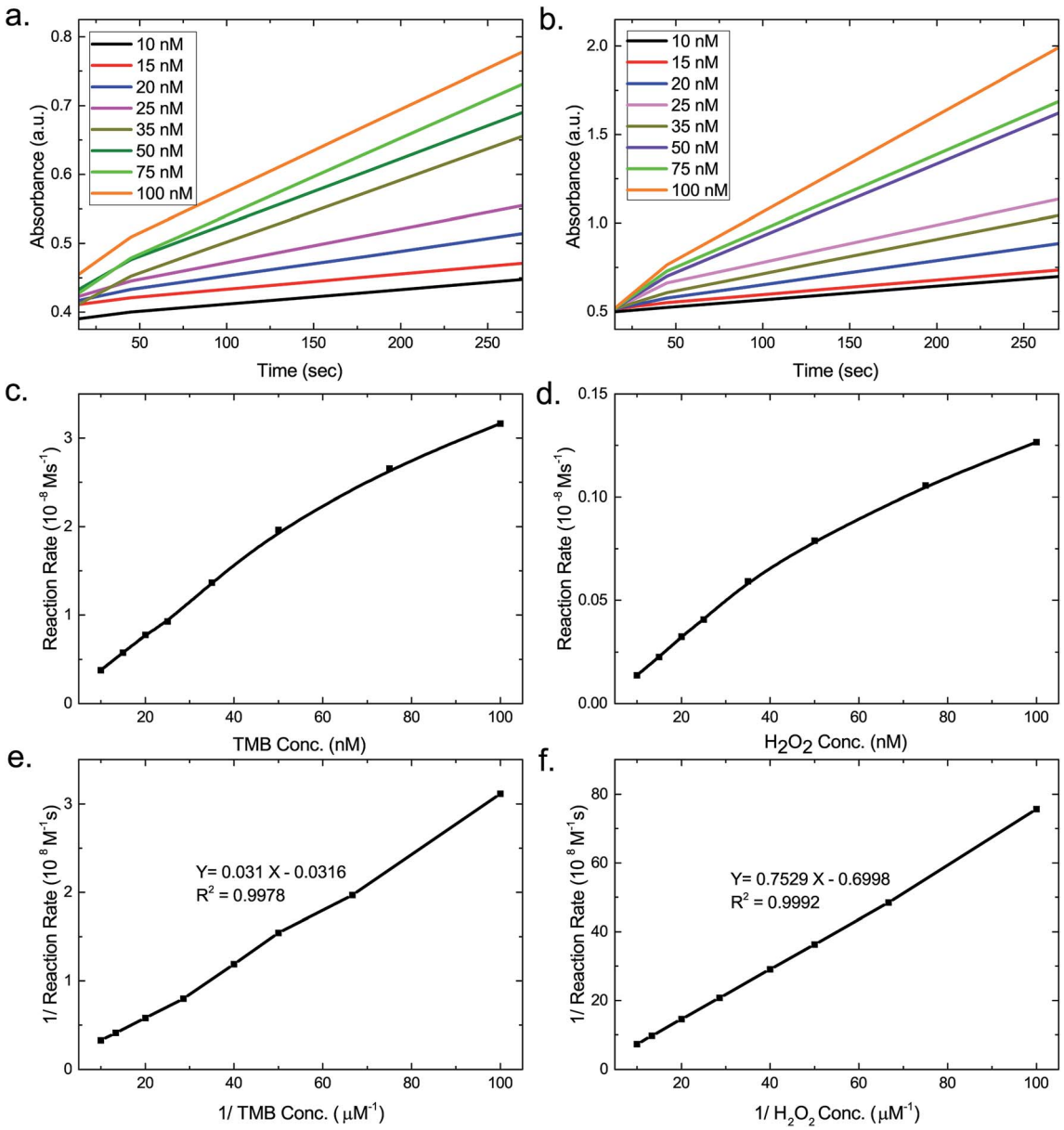

Fig. 4 Time-dependent UV-vis absorption spectra for AuNS@Ag–H–rGO at various concentrations of (a) TMB and (b) H_2O_2 at 652 nm. Michaelis–Menten plot for (c) TMB and (d) H_2O_2. Double reciprocal plots of activity of AuNS@Ag–H–rGO in the presence of different concentrations of (e) TMB and (f) H_2O_2.

Table 1 Kinetic parameters with H_2O_2/TMB as the substrate using different catalysts

	K_M (mM^{-1})		V_{max} (10^{-8} M s^{-1})	
Catalyst	H_2O_2	TMB	H_2O_2	TMB
AuNS@Ag–H–rGO	2.75	0.048	15.3	28.07
AuNP@Ag–H–rGO	2.82	0.062	13.43	21.2
H–rGO–Au[34]	3.1	0.074	12.1	18.1
HRP[10]	3.7	0.434	8.71	10

concentrations of H_2O_2 at 652 nm in presence of AuNP@Ag–H–rGO and AuNS@Ag–H–rGO respectively. The correlation coefficients were calculated to be 0.9983 and 0.9997 representing a good linear behavior. The range of H_2O_2 varied linearly between 10 to 35 nM for both AuNP@Ag–H–rGO and AuNS@Ag–H–rGO, and the limit of detection were obtained as 3.096 nM and 1.26 nM, which are at least an order of magnitude lower than the detection limits reported hitherto (Table S1†).

Mechanism of AuNP/AuNS@Ag–H–rGO as peroxidase mimics

In order to explore a possible mechanism for the catalytic activity of AuNP/AuNS@Ag–H–rGO, an electrochemical study was carried out. Cyclic voltammetry plots were recorded to investigate the catalytic activity of the nanocomposites. Cyclic voltammograms of bare GCE electrode and AuNP/AuNS@Ag–H–rGO modified GCE electrodes in the presence of H_2O_2 are

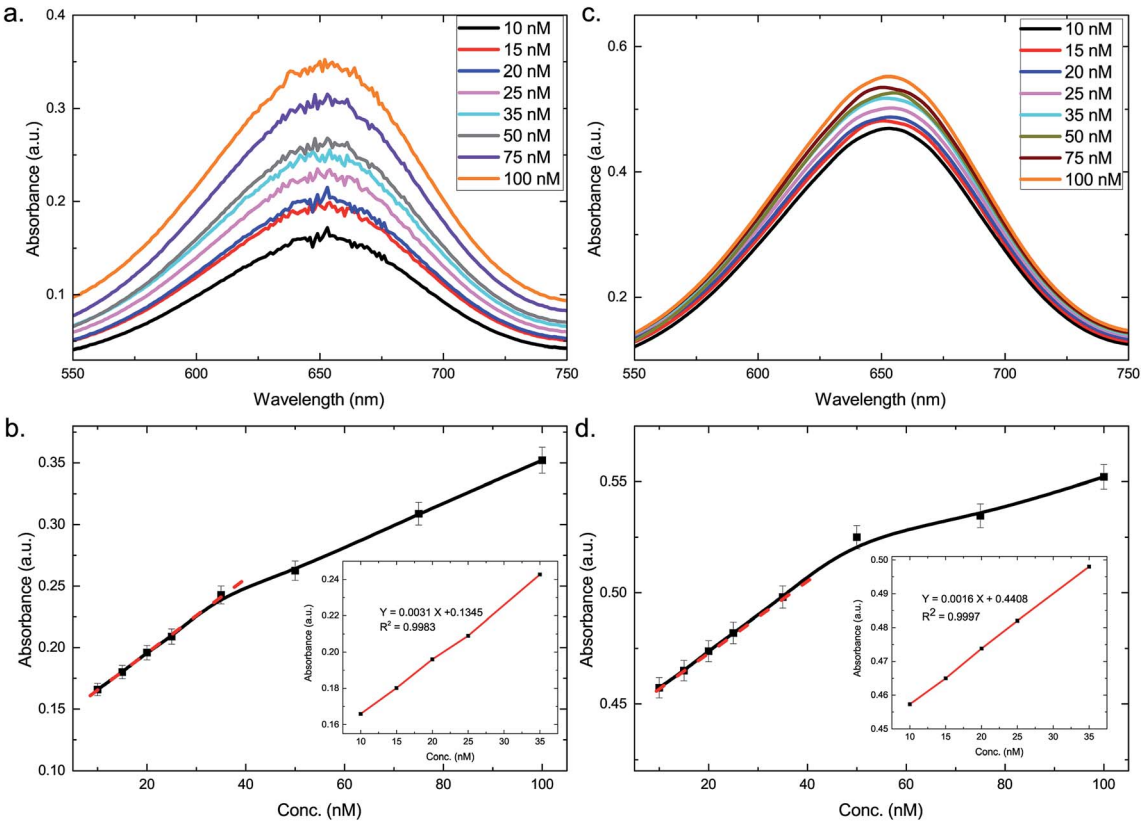

Fig. 5 UV-vis absorption spectra at varying concentrations of H_2O_2 for (a) AuNP@Ag–H–rGO and (c) AuNS@Ag–H–rGO. Response curve for H_2O_2 detection for (b) AuNP@Ag–H–rGO and (d) AuNS@Ag–H–rGO. Insets in (b) and (d) show the linear regression plot for H_2O_2 (1% error bars are shown for data point).

shown in Fig. S11.† The modified electrodes showed higher reduction current as compared to the bare GCE electrodes, suggesting promotion of electron transmission on their surface. An enhancement in the reduction current for the AuNS@Ag–H–rGO modified electrode is a characteristic of its higher electrocatalytic activity for H_2O_2 reduction. The high effective specific area of AuNS and the immobilization of hemin and AuNS@Ag on the rGO sheets, allows for an exposure of highly dense catalytically active centers. This may be conducive to an accelerated surface-confined electron transfer process occurring between the adsorbed TMB and H_2O_2 to efficiently carry out the oxidation of TMB.

Practical implementation of the peroxidase mimetic for glucose detection

Detection in solution form. Taking advantage of the exceptional performance of the AuNS@Ag–H–rGO–TMB system, the proposed assay was further explored by investigating its potential application for detection of glucose. Fig. 6a shows the UV-vis spectra of the resulting solutions after 5 min of adding varying concentrations of glucose. A typical blue color was observed, whose intensity increased with an increase in the concentration of glucose as depicted by the increasing absorbance. Fig. 6b shows the calibration curve of the absorbance change at 652 nm against glucose concentration. The curve was linear in a range from 2 to 5 μM with a correlation coefficient of 0.9986 (inset). The LOD for glucose was calculated to be 425 nM, which is much more sensitive than the previously reported values (1.12 μM,[38] 3.2 μM,[39] 4 μM,[11] and 4.1 μM (ref. 40)). Further, the collected serum samples were analyzed and the glucose concentrations shown in Table 2 were consistent with the results obtained from OneTouch Verio Flex® glucose meter. Hereafter, the serum samples were spiked with known concentrations of glucose (20 μM, 40 μM and 80 μM). Good recoveries were obtained confirming that other entities present in serum had no obvious effect on the catalytic oxidation of TMB demonstrating excellent specificity and selectivity.

Detection on paper-based platform. Paper-based point-of-care diagnostic devices have been widely used owing to their rapid, robust, inexpensive, easy storage and disposability characteristics.[41] To realize the proposed colorimetric detection scheme as a point-of-care diagnostic tool, a paper-based device was fabricated using Whatman filter paper. The test strips (diameter 2 cm) were prepared by soaking them in a 0.5 mL solution of AuNS@Ag–H–rGO. Next, a solution mixture of GOx and TMB was pipetted onto them after which they were dried. Then the human blood serum samples were pipetted on the test strips. Fig. 6c shows the photographs of the test strips after the assay was run. A lower concentration of glucose showed a pale blue color unlike the dark blue coloration observed at higher concentration. The results suggest that the synthesized nanocomposite based paper-based device may be used as a promising platform for on-site rapid detection of glucose.

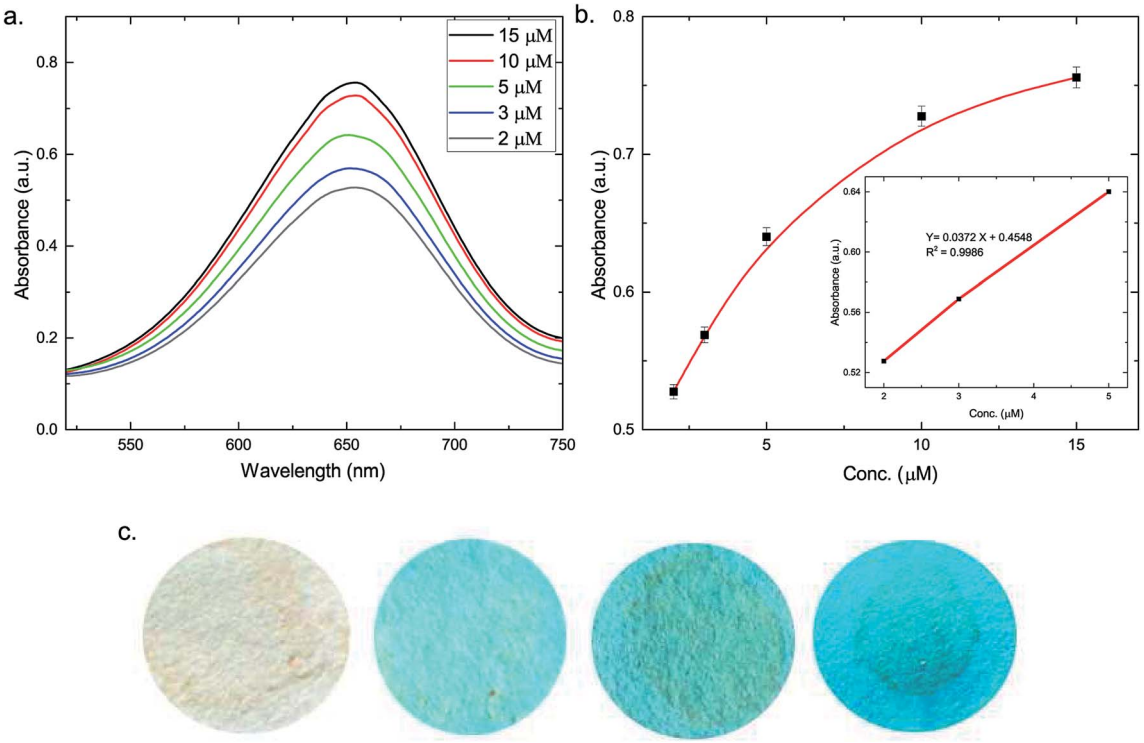

Fig. 6 (a) UV-vis absorption spectra at varying concentrations of glucose in solution for AuNS@Ag–H–rGO. (b) Response curve for glucose detection in solution (1% error bars are shown for data point) and (c) photographs of the test strips (left to right): coated with AuNS@Ag–H–rGO and 5 min after pipetting sample 1, sample 2 and sample 3.

Table 2 Selectivity of the method for determination of determination of glucose in blood serum samples in solution

		Colorimetric method			
Blood sample	OneTouch Verio Flex® glucose meter (mM)	Before spiking (mM)	Spiking concentration (μM)	After spiking (mM)	Recovery (%)
1	3.81	3.64	20	3.59	98.08
2	5.47	5.78	40	5.90	101.3
3	6.95	7.01	80	7.02	99.01

Conclusions

In summary, we report a simple method for the synthesis of a synergistic AuNS@Ag–H–rGO nanocomposite that possesses excellent peroxidase-like activity. The novel nanomimetic exhibits several advantages over HRP such as, high stability, facile synthesis, higher catalytic efficiency, size/shape/composition dependent activity and lower cost. Furthermore, we demonstrate a simple and inexpensive colorimetric method for the detection of hydrogen peroxide and glucose with nanomolar sensitivity. The nanocomposite has also been used to develop a point-of-care diagnostic platform for detection of glucose in human blood serum. The synthesized nanocomposite has immense potential to be utilized extensively in the field of bionanotechnology and medical diagnostics.

Conflict of interest

The authors declare no competing financial interest.

Notes and references

1 D. L. Nelson, A. L. Lehninger and M. M. Cox, *Lehninger principles of biochemistry*, Macmillan, 2008.
2 L. Fruk and C. M. Niemeyer, *Angew. Chem., Int. Ed.*, 2005, **44**, 2603–2606.
3 G. Zhang and P. K. Dasgupta, *Anal. Chem.*, 1992, **64**, 517–522.
4 T. Xue, S. Jiang, Y. Qu, Q. Su, R. Cheng, S. Dubin, C. Y. Chiu, R. Kaner, Y. Huang and X. Duan, *Angew. Chem.*, 2012, **124**, 3888–3891.
5 Z. Liu, R. Cai, L. Mao, H. Huang and W. Ma, *Analyst*, 1999, **124**, 173–176.

6 R. P. Bonar-Law and J. K. Sanders, *J. Am. Chem. Soc.*, 1995, **117**, 259–271.
7 Y. Song, K. Qu, C. Zhao, J. Ren and X. Qu, *Adv. Mater.*, 2010, **22**, 2206–2210.
8 F. Qu, T. Li and M. Yang, *Biosens. Bioelectron.*, 2011, **26**, 3927–3931.
9 H. Jiang, Z. Chen, H. Cao and Y. Huang, *Analyst*, 2012, **137**, 5560–5564.
10 L. Gao, J. Zhuang, L. Nie, J. Zhang, Y. Zhang, N. Gu, T. Wang, J. Feng, D. Yang and S. Perrett, *Nat. Nanotechnol.*, 2007, **2**, 577–583.
11 Y. Jv, B. Li and R. Cao, *Chem. Commun.*, 2010, **46**, 8017–8019.
12 K. Yoshizumi, K. Aoki, I. Nouchi, T. Okita, T. Kobayashi, S. K. Amakura and M. Tajima, *Atmos. Environ.*, 1984, **18**, 395–401.
13 T. C. Bruice, *Acc. Chem. Res.*, 1991, **24**, 243–249.
14 F. Bedioui, *Coord. Chem. Rev.*, 1995, **144**, 39–68.
15 L. Shao, A. S. Susha, L. S. Cheung, T. K. Sau, A. L. Rogach and J. Wang, *Langmuir*, 2012, **28**, 8979–8984.
16 H. Wei, S. M. H. Abtahi and P. J. Vikesland, *Environ. Sci.: Nano*, 2015, **2**, 120–135.
17 H.-H. Deng, G.-L. Hong, F.-L. Lin, A.-L. Liu, X.-H. Xia and W. Chen, *Anal. Chim. Acta*, 2016, **915**, 74–80.
18 W. Luo, C. Zhu, S. Su, D. Li, Y. He, Q. Huang and C. Fan, *ACS Nano*, 2010, **4**, 7451–7458.
19 L. Zhang and L. Li, *Anal. Methods*, 2016, **8**, 6691–6695.
20 X. Zhang, M. Wei, B. Lv, Y. Liu, X. Liu and W. Wei, *RSC Adv.*, 2016, **6**, 35001–35007.
21 L.-L. Wu, L.-Y. Wang, Z.-J. Xie, F. Xue and C.-F. Peng, *RSC Adv.*, 2016, **6**, 75384–75389.
22 T. Vo-Dinh, *TrAC, Trends Anal. Chem.*, 1998, **17**, 557–582.
23 L. Lu, K. Ai and Y. Ozaki, *Langmuir*, 2008, **24**, 1058–1063.
24 A. M. Fales, H. Yuan and T. Vo-Dinh, *J. Phys. Chem. C*, 2014, **118**, 3708–3715.
25 J.-S. Lee, A. K. Lytton-Jean, S. J. Hurst and C. A. Mirkin, *Nano Lett.*, 2007, **7**, 2112.
26 X. Wang, Z. Zhang and G. V. Hartland, *J. Phys. Chem. B*, 2005, **109**, 20324–20330.
27 L. Song, C. Huang, W. Zhang, M. Ma, Z. Chen, N. Gu and Y. Zhang, *Colloids Surf., A*, 2016, **506**, 747–755.
28 B. Garg, T. Bisht and Y.-C. Ling, *Molecules*, 2015, **20**, 14155–14190.
29 A. D. Association, *Diabetes Care*, 2014, **37**, S81–S90.
30 T. N. Seyfried, R. E. Flores, A. M. Poff and D. P. D'Agostino, *Carcinogenesis*, 2014, **35**, 515–527.
31 K. Yang, L. Feng, H. Hong, W. Cai and Z. Liu, *Nat. Protoc.*, 2013, **8**, 2392–2403.
32 X. Jiang, Y. Chai, H. Wang and R. Yuan, *Biosens. Bioelectron.*, 2014, **54**, 20–26.
33 N. G. Bastús, J. Comenge and V. Puntes, *Langmuir*, 2011, **27**, 11098–11105.
34 X. Lv and J. Weng, *Sci. Rep.*, 2013, **3**, 3285.
35 M. Tsuji, M. Matsunaga, H. Kumagai, M. Ogino, S. Hikino, Y. Yoshida and T. Ishizaki, *CrystEngComm*, 2013, **15**, 1345–1351.
36 L. A. Marquez and H. B. Dunford, *Biochemistry*, 1997, **36**, 9349–9355.
37 D. Porter and H. Bright, *J. Biol. Chem.*, 1983, **258**, 9913–9924.
38 N. Lu, M. Zhang, L. Ding, J. Zheng, C. Zeng, Y. Wen, G. Liu, A. Aldalbahi, J. Shi and S. Song, *Nanoscale*, 2017, **9**, 4508–4515.
39 C. Lu, X. Liu, Y. Li, F. Yu, L. Tang, Y. Hu and Y. Ying, *ACS Appl. Mater. Interfaces*, 2015, **7**, 15395–15402.
40 A. Dalui, B. Pradhan, U. Thupakula, A. H. Khan, G. S. Kumar, T. Ghosh, B. Satpati and S. Acharya, *Nanoscale*, 2015, **7**, 9062–9074.
41 A. W. Martinez, S. T. Phillips, G. M. Whitesides and E. Carrilho, *Anal. Chem.*, 2009, **82**, 3–10.